Supporting Information: Revealing Ultrafast Population Transfer Between Nearly Degenerated Electronic States

Pascal Heim,[†,§] Sebastian Mai,[‡,¶,§] Bernhard Thaler,[†] Stefan Cesnik,[†] Davide Avagliano,[‡] Dimitra Bella-Velidou,[‡] Wolfgang E. Ernst,[†] Leticia González,[*,‡] and Markus Koch[*,†]

†*Graz University of Technology, Institute of Experimental Physics, Petersgasse 16, A-8010 Graz, Austria*

‡*University of Vienna, Faculty of Vienna, Institute of Theoretical Chemistry, Währinger Str. 17, A-1090 Vienna, Austria*

¶*Present Address: Vienna University of Technology, Photonics Institute, Gußhausstr. 27–29, A-1040 Vienna, Austria*

§*These authors contributed equally to this work*

E-mail: leticia.gonzalez@univie.ac.at; markus.koch@tugraz.at

Contents

S1 Kinetic Model

We describe the population dynamics by the following differential equation system of a unimolecular first-order kinetic model:

$$\frac{\partial}{\partial t}\vec{P} = \mathbf{M}\vec{P} + g(t)\vec{P}_0, \tag{1}$$

with the time-dependent population vector $\vec{P}$:

$$\vec{P} = \begin{pmatrix} P_{\mathrm{n3p_x}}(t) \\ P_{\mathrm{n3p_y}}(t) \\ P_{\mathrm{n3p_z}}(t) \\ P_{\pi\pi^*}(t) \end{pmatrix} \tag{2}$$

where $P_{\pi\pi^*}(t)$ also includes other dark states besides the $\pi\pi^*$. The coupling matrix $\mathbf{M}$ is:

$$\mathbf{M} = \begin{pmatrix} -\frac{1}{\tau_{\mathrm{xy}}} - \frac{1}{\tau_{\mathrm{xz}}} - \frac{1}{\tau_{\mathrm{x}\pi}} & +\frac{1}{\tau_{\mathrm{yx}}} & +\frac{1}{\tau_{\mathrm{zx}}} & 0 \\ +\frac{1}{\tau_{\mathrm{xy}}} & -\frac{1}{\tau_{\mathrm{yx}}} - \frac{1}{\tau_{\mathrm{yz}}} - \frac{1}{\tau_{\mathrm{y}\pi}} & +\frac{1}{\tau_{\mathrm{zy}}} & 0 \\ +\frac{1}{\tau_{\mathrm{xz}}} & +\frac{1}{\tau_{\mathrm{yz}}} & -\frac{1}{\tau_{\mathrm{zx}}} - \frac{1}{\tau_{\mathrm{zy}}} - \frac{1}{\tau_{\mathrm{z}\pi}} & 0 \\ +\frac{1}{\tau_{\mathrm{x}\pi}} & +\frac{1}{\tau_{\mathrm{y}\pi}} & +\frac{1}{\tau_{\mathrm{z}\pi}} & 0 \end{pmatrix}. \tag{3}$$

This matrix assumes that the n3p states couple to each other and decay to the $\pi\pi^*$ state, but we neglect population transfer from the $\pi\pi^*$ back to the n3p states. The term $g(t)\vec{P}_0$ in equation (1) is the source term that populates the states. It is the product of the normalized temporal profile of the laser excitation $g(t)$ and a state-dependent prefactor $\vec{P}_0$ that depends on the relevant transition dipole moments.

Equation (1) can be solved by convolution of the impulse response function of the linear differential equation with the source term:

$$\vec{P}(t) = g(t) \circledast \left(\Theta(t)e^{\mathbf{M}t}\right) \cdot \vec{P}_0 \tag{4}$$

If the matrix $\mathbf{M}$ is diagonalizable, i.e., $\mathbf{M} = \mathbf{V}\mathbf{\Lambda}\mathbf{V}^{-1}$, one can rewrite this equation as:

$$\vec{P}(t) = g(t) \circledast \left(\Theta(t)\mathbf{V}e^{\mathbf{\Lambda}t}\mathbf{V}^{-1}\right) \cdot \vec{P}_0, \tag{5}$$

with the eigenvalue matrix $\hat{\Lambda} = \mathrm{diag}(\lambda_1, \lambda_2, \cdots) = \mathrm{diag}(\tau_1^{-1}, \tau_2^{-1}, \cdots)$. The latter equation can be rewritten for the population of a single state as:

$$P_i(t) = \sum_m \sum_n g(t) \circledast \left(\Theta(t)e^{\frac{t}{\tau_m}}\right) V_{im}V_{mn}^{-1}P_{0,n}. \tag{6}$$

We note here that the coupling matrix $\mathbf{M}$ might have complex eigenvalues. Below, for the fits of the experimental time-resolved photoelectron spectrum, only real time constants were fitted. For the theoretical results, where the full coupling matrix is available, in few cases the eigenvalues were found to be complex. However, the imaginary part in the time constants was generally small (below 10% of the real part), and hence was neglected.

S1.1 Fitting function for experimental data

The measured signal $S(E, t)$ depends on the photoelectron energy (E) and the time delay between pump and probe pulses (t). It can be described[S1] as the sum over the products of the spectral shape

of each state $\sigma_i(E)$, which also includes the ionization cross section, and time dependent population P_i of each state convoluted with the temporal shape of the probe pulse $g'(t)$:

$$S(E,t) = g'(t) \circledast \sum_i P_i(t)\sigma_i(E) \tag{7}$$

Inserting equation (6) into (7) and separating the time-dependent and time-independent parts lead to:

$$S(E,t) = \sum_m \underbrace{g'(t) \circledast g(t) \circledast \left(\Theta(t)e^{\lambda_m t}\right)}_{f_m(t)} \underbrace{\sum_i \sum_n V_{im}V^{-1}_{mn}P_{0,n}\sigma_i(E)}_{\mathrm{DAS}_m(E)}. \tag{8}$$

Equation (8) is the basis for the definition of the fitting function that we employed for the global 2D fit of the experimental time-resolved photoelectron spectra. We assume a Gaussian shape for the pump pulse $g(t)$ and the probe pulse $g'(t)$, therefore the convolution of the pump and the probe pulse is also a Gaussian function. The temporal width of the resulting Gaussian function $g(t) \circledast g'(t)$ was determined by the fit to be 50–90 fs, depending on the excitation photon energy. To account for a cross correlation signal around $t = 0\,\mathrm{fs}$, we also added a Gaussian function times a "cross correlation spectrum" (CCS).

$$S^{\mathrm{Gaussian}}(E,t) = G(t)\mathrm{CCS}(E) \tag{9}$$

The optimal maximum number of m in equation (8) was found by varying the maximum number of m until we obtained a satisfactory fit without overfitting. The best fit was obtained with $m = \{1, 2\}$.

We note here that the decay associated spectrum (DAS) in equation (8) are in general very difficult to interpret, because they depend on the initial populations and on the eigenvectors of the coupling matrix. Hence, only in the special cases of purely sequential or parallel kinetic models,[S2] the DAS can be directly linked to the underlying spectra of the electronic states $\sigma_i(E)$. Opposite signs of different DAS at the same energy are indicative of population transfer from one state to another, but determining the amount of population flux is only possible in a purely sequential model, which is not applicable in our case. Therefore, a closer interpretation of our DAS is not possible.

S2 Calibration of photoelectron spectra

We calibrate our photoelectron (PE) spectra based on the energy of the $n3p_z$ state, E_{n3p_z}, as determined by high-resolution synchrotron measurements.[S3] The measured PE energy, E_{PE} is calculated from

$$E_{PE} = \hbar\omega_{probe} + E_{n3pz} - E_{IP},$$

where $\hbar\omega_{probe}$ is the probe photon energy and E_{IP} is the adiabatic acetone ionization potential (E_{IP}=9.708 eV[S3]). This is necessary because the retarding voltage applied to increase the energy resolution causes some uncertainty of the measured PE kinetic energy, which depends on the exact potential at the location of ionization. Our calibration assumes that the potential energy surfaces of the excited and ionic states are parallel. Therefore we take the $n3p_z$ state as reference, since the $n3p_y$ is distorted due to coupling to the $\pi\pi^*$ state and the $n3p_x$ is populated in high vibrational states.

S3 Additional Experimental Results

In the following, we present the experimental results for different excitation wavelengths from 320 nm to 336 nm. We show the transient photoelectron spectra, the 2D global fit with two time constants and Gaussian cross correlation function, the corresponding DAS, and the residua of the fit.

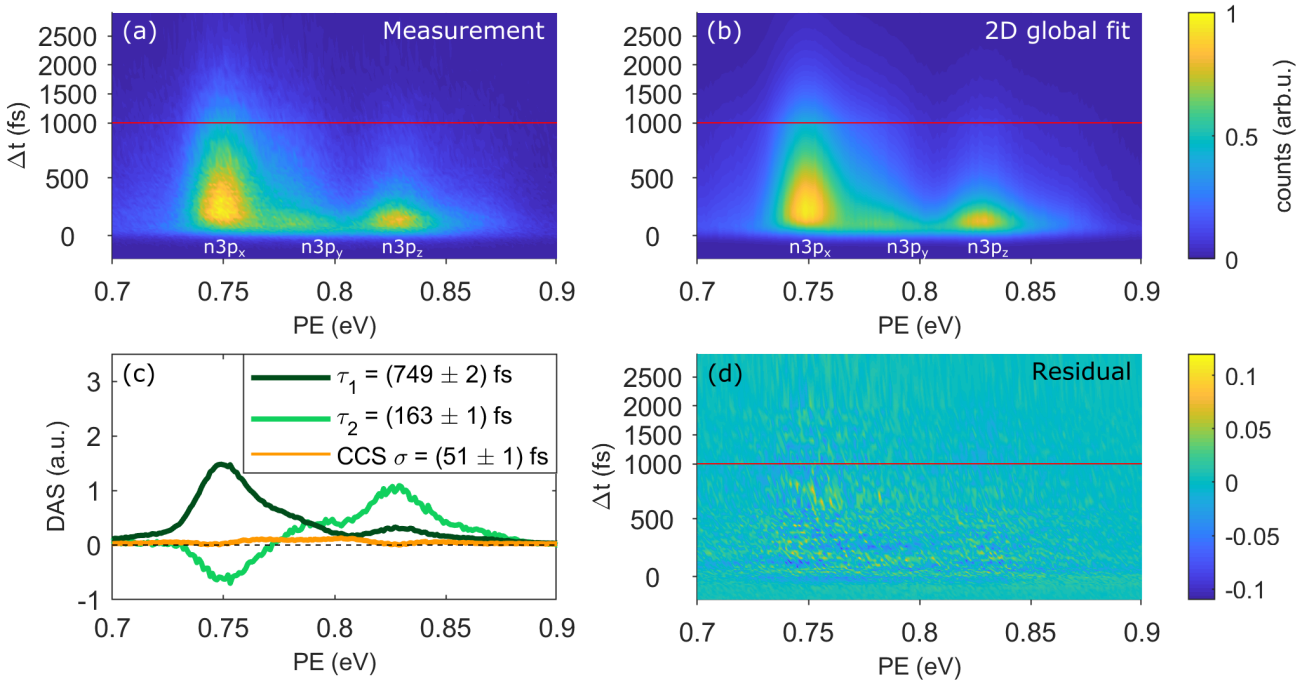

Figure S1: Measured photoelectron spectrum (a), its 2D global fit (b) with the corresponding DAS time constants and CCS with standard deviation of the Gaussian cross-correlation function (c) and residuals (d). Excitation wavelength is 320 nm. The red lines in (a), (b) and (c) indicate a change of the vertical scale.

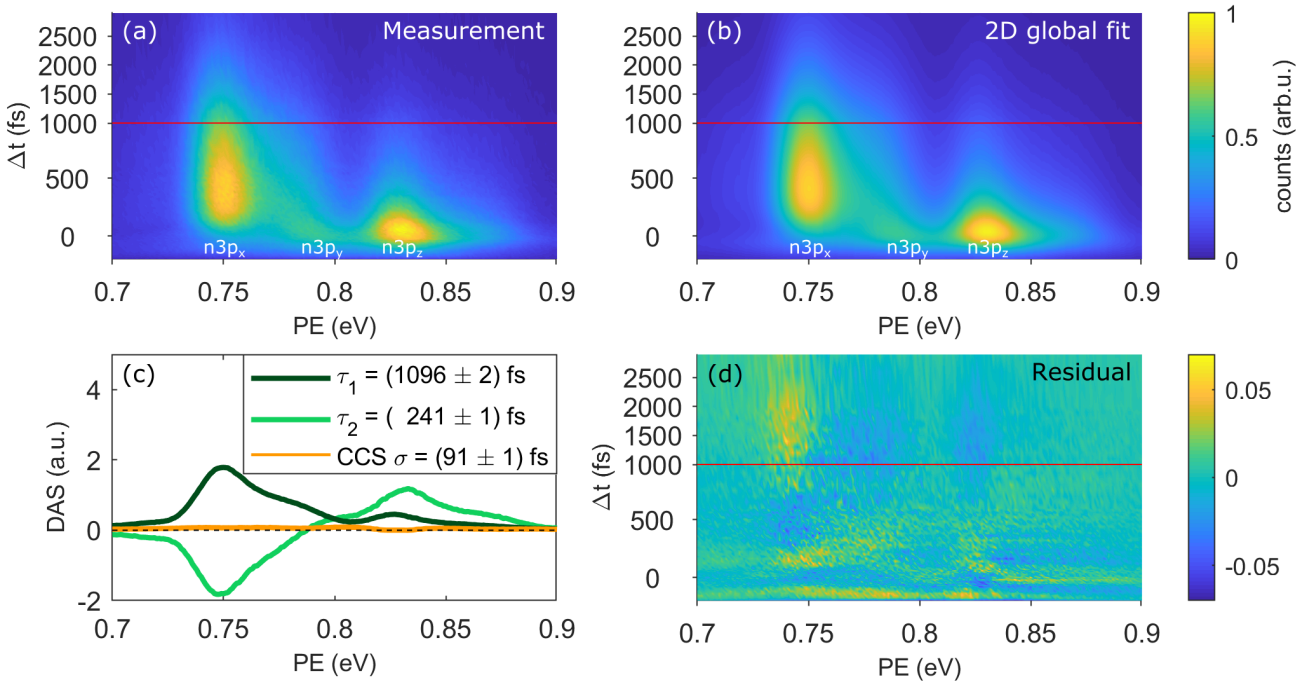

Figure S2: Measured photoelectron spectrum (a), its 2D global fit (b) with the corresponding DAS time constants and CCS with standard deviation of the Gaussian cross-correlation function (c) and residuals (d). Excitation wavelength is 324 nm. The red lines in (a), (b) and (c) indicate a change of the vertical scale.

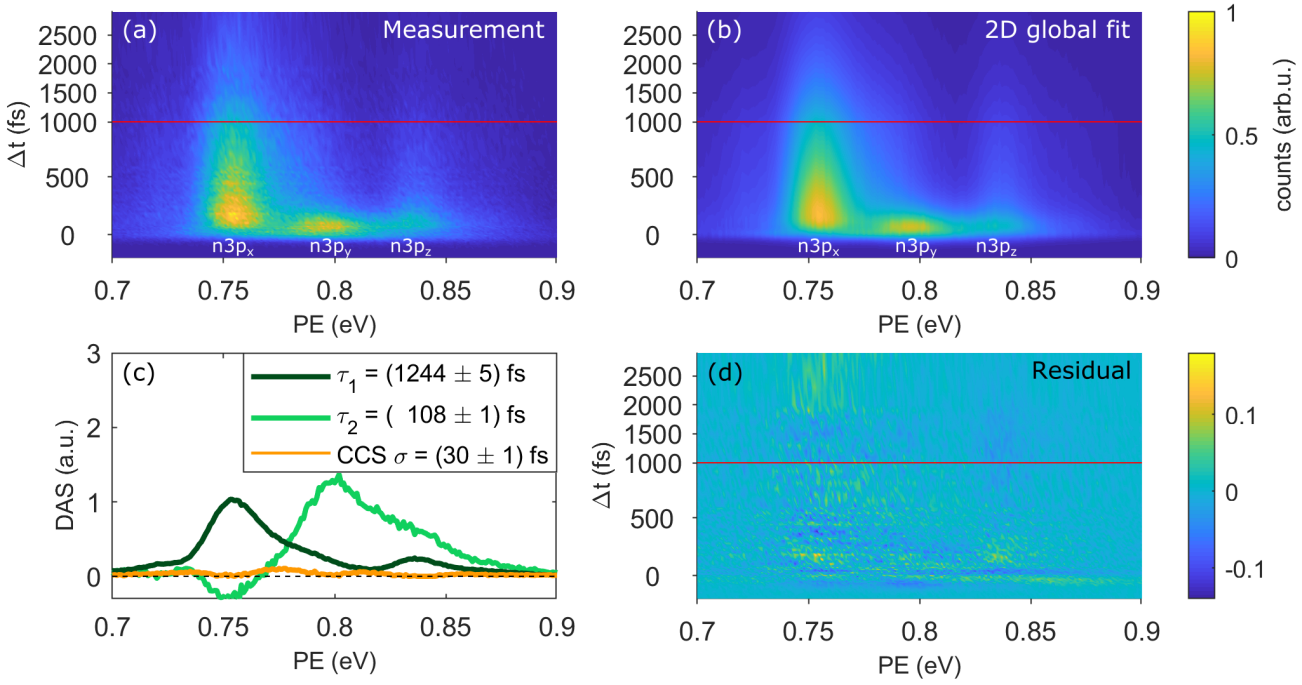

Figure S3: Measured photoelectron spectrum (a), its 2D global fit (b) with the corresponding DAS time constants and CCS with standard deviation of the Gaussian cross-correlation function (c) and residuals (d). Excitation wavelength is 329 nm. The red lines in (a), (b) and (c) indicate a change of the vertical scale.

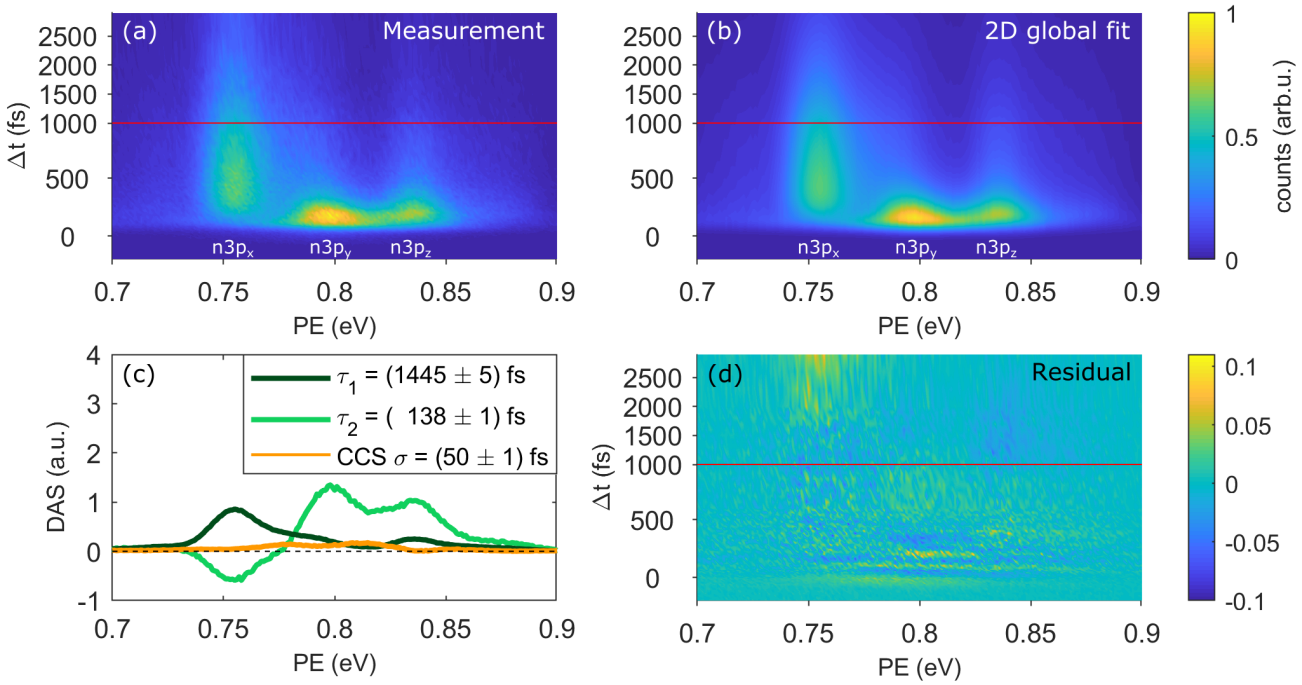

Figure S4: Measured photoelectron spectrum (a), its 2D global fit (b) with the corresponding DAS time constants and CCS with standard deviation of the Gaussian cross-correlation function (c) and residuals (d). Excitation wavelength is 333 nm. The red lines in (a), (b) and (c) indicate a change of the vertical scale.

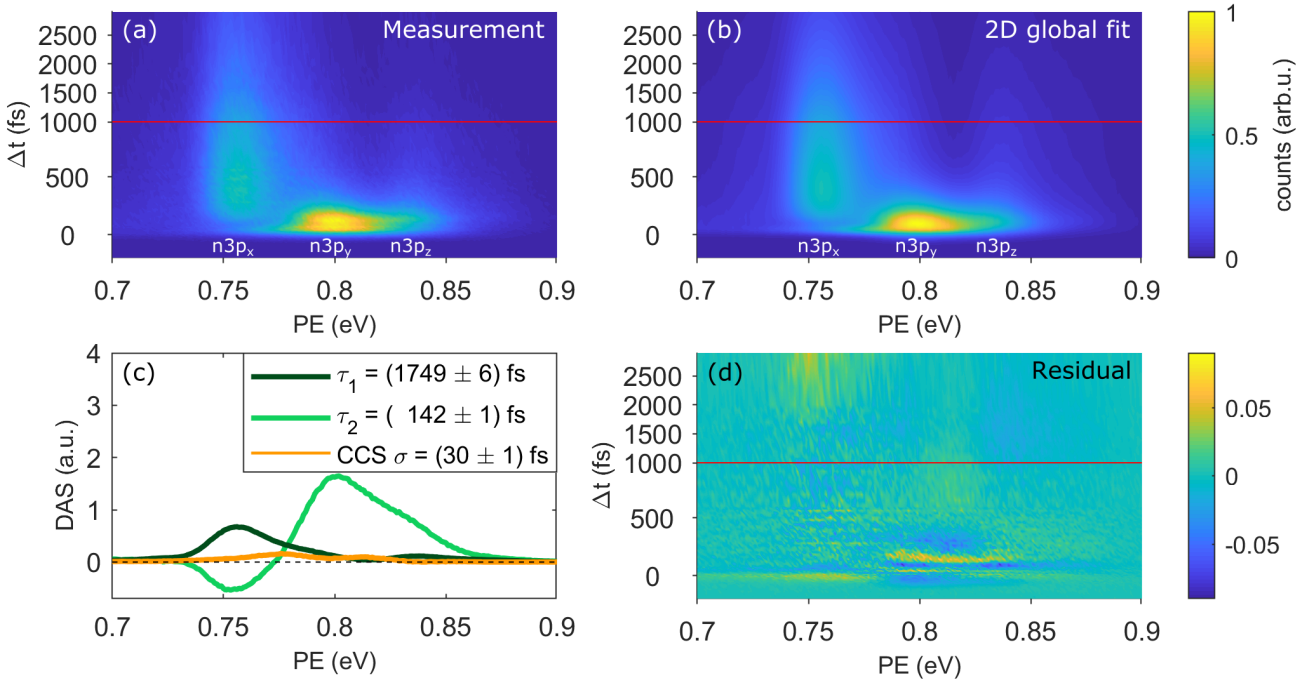

Figure S5: Measured photoelectron spectrum (a), its 2D global fit (b) with the corresponding DAS time constants and CCS with standard deviation of the Gaussian cross-correlation function (c) and residuals (d). Excitation wavelength is 336 nm. The red lines in (a), (b) and (c) indicate a change of the vertical scale.

S4 Computational Details

S4.1 The linear vibronic coupling model

In this work, we employ a linear vibronic coupling (LVC) model[S4,S5] to describe the coupled potential energy surfaces of the electronic states of acetone. An LVC model is a Taylor expansion of the potential energy surfaces around a reference geometry (e.g., the minimum of a representative state), expanded in normal mode coordinates. The mass-frequency-weighted normal mode coordinate Q_i of mode i is defined (in atomic units) as:

$$Q_i = \sqrt{\omega_i} \sum_{A}^{\text{atoms}} K_{Ai} \sqrt{M_A} (R_A - R_A^{\text{ref}}), \tag{10}$$

where ω_i is the normal-mode frequency, K_{Ai} are elements of the Cartesian-normal mode transformation matrix, M_A are the atomic masses, and R_A are the Cartesian coordinates of the molecule.

The matrix of the electronic Hamiltonian is given by:

$$\mathbf{H}(\vec{Q}) = \mathbf{1} V_0(\vec{Q}) + \mathbf{W}(\vec{Q}). \tag{11}$$

The reference potential V_0 is identical for all electronic states, and in the present work given by the harmonic potential

$$V_0(\vec{Q}) = \sum_{i}^{\text{modes}} \frac{\omega_i}{2} Q_i^2. \tag{12}$$

The coupling matrix $\mathbf{W}(\vec{Q})$ serves to create the individual potential energy surfaces from the reference potential, and consists of constant and linear terms:

$$W_{\alpha\alpha}(\vec{Q}) = \epsilon_\alpha + \sum_{i}^{\text{modes}} \kappa_i^\alpha Q_i \tag{13}$$

and

$$W_{\alpha\beta}(\vec{Q}) = \sum_{i}^{\text{modes}} \lambda_i^{\alpha\beta} Q_i, \tag{14}$$

where ϵ_α are the excitation energies at the reference geometry, κ_i^α are the gradients at the reference geometry, and $\lambda_i^{\alpha\beta}$ are the linear intrastate coupling constants. In this way, the Hamiltonian matrix $\mathbf{H}(\vec{Q})$ is given in a diabatic representation; a diagonalization of $\mathbf{H}(\vec{Q})$ then produces the adiabatic potential energy surfaces that we are employing for our dynamics simulations.

S4.2 Electronic structure calculations

In order to find the parameter values for the LVC model, we employed the spin-opposite scaling variant of the algebraic diagrammatic construction scheme for the polarization propagator to second order (SOS-ADC(2)) method.[S6] The basis set, which needs to be able to describe a large set of high-lying Rydberg orbitals, was cc-pVTZ[S7] for O and C, cc-pVDZ[S7] for H, and an additional $10s8p6d4f$ Rydberg basis set[S8] centered on the O atom. All electronic structure calculations were carried out with Turbomole 7.0.[S9] Wave function overlaps between ADC(2) wave functions, needed to obtain the λ parameters,[S10] were computed with the WFoverlap code.[S11] The molecule was oriented such that the z axis is parallel to the molecular axis and the x axis perpendicular to the molecular plane.

S4.3 Parametrization of LVC model

The reference potential V_0 is fully specified with the masses M_A and the parameters ω_i and K_{Ai}. These were obtained from a frequency calculation for the $n3s$ state at the SOS-ADC(2) level of theory. The $n3s$ state was chosen as it is well separated from other states and hence easy to optimize, but also parallel to the higher Rydberg states and therefore a better reference state than the S_0. We used all 24 normal modes of acetone (resulting in 720 K_{Ai} elements and 24 ω_i parameters). An overview over the modes and the values of ω_i are given in Table S1.

The ϵ and κ parameters were obtained from a single-point calculation at the reference geometry ($n3s$ minimum). The ϵ parameters are the vertical excitation energies at that geometry, and the κ parameters are the gradients of the states transformed into the normal-mode basis. To obtain the λ parameters, we employed a numerical differentiation scheme[S10] that requires two extra calculations for each normal mode and the computation of wave function overlaps between the states at the reference geometry and the displaced geometries.

Our LVC model contains 49 singlet state, which is necessary to include the $\pi\pi^*$ state that is very high in energy at the reference geometry. Based on the numbers and symmetries of the states ($12A_1$, $11A_2$, $5B_1$, $21B_2$) and normal modes ($8a_1$, $4a_2$, $5b_1$, $7b_2$), this LVC model contains 49 ϵ parameters, 392 non-zero κ parameters, and 7280 non-zero λ parameters. See Table S2 for the ϵ values of all states, and Table S3 for the κ parameters. All parameters can be found in the supplementary files.

Table S1: Normal modes for the $n3s$ state at the SOS-ADC(2) level of theory.

Mode[a]	Character	Symmetry	ω (cm^{-1})
7	Methyl rotation asym	a_2	50.3
8	Methyl rotation sym	b_1	161.0
9	CCC bend	a_1	324.3
10	CCO bend inplane	b_2	359.0
11	O=CCC bend out of plane	b_1	565.6
12	C-C stretch sym	a_1	757.2
13	Methyl wagging asym	a_2	887.9
14	Methyl wagging in plane	b_2	939.5
15	Methyl wagging out of plane	b_1	1072.7
16	Methyl wagging sym + C=O stretch	a_1	1073.9
17	C-C stretch asym	b_2	1143.7
18	Methyl breath + C=O stretch	a_1	1234.4
19	Methyl breath	b_2	1323.2
20	Methyl breath sym	a_1	1422.9
21	Methyl breath asym	b_2	1423.6
22	Methyl scissoring asym	a_2	1431.9
23	Methyl scissoring sym + C=O stretch	a_1	1440.2
24	Methyl scissoring out of plane	b_1	1460.8
25	C-H stretch	b_2	2952.9
26	C-H stretch	a_1	2961.7
27	C-H stretch	a_2	3056.5
28	C-H stretch	b_1	3118.2
29	C-H stretch	a_1	3160.1
30	C-H stretch	b_2	3167.3

[a] Numbering includes translational and rotational degrees of freedom to be consistent with the supplementary files containing the K_{Ai} and λ parameters.

Table S2: Electronic states of acetone at the SOS-ADC(2) level of theory. State ordering and energies refer to the S_0 minimum at MP2 level of theory. The ϵ parameters refer to the $n3s$ minimum at SOS-ADC(2) level of theory. The $\Delta E_{\mathbf{vert}}$ column provides the vertical excitation energies from the S_0 minimum.

State	Character	Symmetry	ϵ (eV)	ΔE_{vert} (eV)
S_0	closed shell	A_1	0.00	0.00
S_1	$n\pi$	A_2	4.23	4.52
S_2	$n3s$	B_2	6.22	6.56
S_3	$n3p_x$	A_2	7.05	7.37
S_4	$n3p_y$	A_1	7.09[a]	7.41
S_5	$n3p_z$	B_2	7.15	7.45
S_6	$n3d_{x^2-y^2}$	B_2	7.51	7.87
S_7	$n3d_{yz}$	A_1	7.74	8.05
S_8	$n3d_{xz}$	A_2	7.75	8.08
S_9	$n3d_{xy}$	B_1	7.77	8.10
S_{10}	$n3d_{z^2}$	B_2	7.79	8.11
S_{11}	$n4s$	B_2	7.83	8.16
S_{12}	$n4p_x$	A_2	8.02	8.35
S_{13}	$n4p_z$	B_2	8.06	8.39
S_{14}	$n4p_y$	A_1	8.07	8.40
S_{15}	$n4d_{x^2-y^2}$	B_2	8.18	8.52
S_{16}	$n4d_{yz}$	A_1	8.29	8.61
S_{17}	$n4d_{xz}$	A_2	8.28	8.61
S_{18}	$n4d_{xy}$	B_1	8.30	8.63
S_{19}	$n4d_{z^2}$	B_2	8.31	8.64
S_{20}	$n5s$	B_2	8.32	8.65
S_{21}	$n5p_x$	A_2	8.40	8.73
S_{22}	$n5p_y$	A_1	8.41	8.74
S_{23}	$n5p_z$	B_2	8.42	8.75
S_{24}	$n4f$	A_2	8.43	8.75
S_{25}	$n4f$	B_2	8.43	8.75
S_{26}	$n4f$	A_1	8.43	8.76
S_{27}	$n4f$	B_1	8.44	8.77
S_{28}	$n4f$	A_1	8.46	8.79
S_{29}	$n4f$	B_2	8.48	8.80
S_{30}	$n4f$	A_2	8.48	8.80
S_{31}	$n6s$	B_2	8.50	8.83
S_{32}	$n\sigma$	B_2	8.59	8.92
S_{33}	$n6p_x$	A_2	8.61	8.95
S_{34}	$n6p_z$	B_2	8.63	8.96
S_{35}	$n6p_y$	A_1	8.62	8.96
S_{36}	$n5d_{xz}$	A_2	8.64	8.98
S_{37}	$n5d_{yz}$	A_1	8.65	8.98
S_{38}	$n5d_{xy}$	B_1	8.66	8.99
S_{39}	$n5d_{x^2-y^2}$	B_2	8.67	9.00
S_{40}	$n5d_{z^2}$	B_2	8.68	9.01
S_{41}	?	B_2	8.74	9.07
S_{42}	?	B_2	8.83	9.17
S_{43}	$n7p_x$	A_2	8.94	9.27
S_{44}	$n7p_z$	B_2	8.98	9.31
S_{45}	?	B_1	8.81	9.32
S_{46}	$n7p_y$	A_1	9.01	9.34
S_{47}	?	B_2	9.02	9.37
S_{48}	$\pi\pi^*$	A_1	8.77	9.51

[a] This value was decreased manually (from 7.14 eV) to fit the experimental excitation energy of $n3p_y$.

Table S3: All non-zero κ parameters in the LVC model (meV). Note that for the reference state, S_2, all κ values are zero.

State	Character	κ_9	κ_{12}	κ_{16}	κ_{18}	κ_{20}	κ_{23}	κ_{26}	κ_{29}
S_0	closed shell	52	-39	78	37	-40	218	-17	9
S_1	$n\pi$	-14	-53	261	-285	-54	-125	-6	14
S_2	$n3s$	0	0	0	0	0	0	0	0
S_3	$n3p_x$	-17	-8	14	-5	-14	12	-50	14
S_4	$n3p_y$	-19	-5	12	-40	-24	23	-30	5
S_5	$n3p_z$	-16	-5	11	-34	8	39	-42	8
S_6	$n3d_{x^2-y^2}$	-11	2	-7	-15	-28	-11	-14	20
S_7	$n3d_{yz}$	-22	-7	15	-34	-2	32	-35	17
S_8	$n3d_{xz}$	-21	-4	9	-26	-1	25	-27	6
S_9	$n3d_{xy}$	-20	-5	14	-29	-13	17	-39	11
S_{10}	$n3d_{z^2}$	-23	-4	13	-35	-7	26	-35	10
S_{11}	$n4s$	-23	-4	14	-38	-4	19	-31	20
S_{12}	$n4p_x$	-20	-3	18	-33	-10	13	-39	10
S_{13}	$n4p_z$	-21	-4	17	-43	-4	21	-38	9
S_{14}	$n4p_y$	-20	-3	23	-49	-13	13	-31	7
S_{15}	$n4d_{x^2-y^2}$	-18	0	12	-36	-16	4	-27	14
S_{16}	$n4d_{yz}$	-22	-4	20	-44	-6	19	-35	13
S_{17}	$n4d_{xz}$	-22	-3	14	-40	-4	17	-30	8
S_{18}	$n4d_{xy}$	-21	-3	19	-41	-10	14	-37	11
S_{19}	$n4d_{z^2}$	-25	-2	19	-42	-4	19	-35	10
S_{20}	$n5s$	-23	-3	17	-46	-9	14	-33	19
S_{21}	$n5p_x$	-22	-3	19	-42	-10	13	-36	10
S_{22}	$n5p_y$	-23	-3	24	-49	-12	9	-31	8
S_{23}	$n5p_z$	-24	-3	20	-45	-7	17	-36	10
S_{24}	$n4f$	-22	-4	16	-38	-11	17	-37	10
S_{25}	$n4f$	-22	-4	18	-39	-6	21	-35	14
S_{26}	$n4f$	-22	-2	21	-48	-11	13	-34	10
S_{27}	$n4f$	-24	-3	17	-38	-9	22	-34	9
S_{28}	$n4f$	-24	-3	19	-42	-9	20	-36	10
S_{29}	$n4f$	-23	-2	18	-37	-9	21	-36	10
S_{30}	$n4f$	-22	-2	18	-38	-9	21	-36	10
S_{31}	$n6s$	-19	0	18	-43	-12	7	-31	10
S_{32}	$n\sigma$	-24	-2	17	-47	-13	9	-32	21
S_{33}	$n6p_x$	-22	-2	20	-45	-9	11	-36	10
S_{34}	$n6p_z$	-23	-2	20	-49	-3	15	-35	8
S_{35}	$n6p_y$	-19	3	60	-99	-5	-25	-24	9
S_{36}	$n5d_{xz}$	-22	-2	14	-39	-4	17	-29	7
S_{37}	$n5d_{yz}$	-23	-4	21	-45	-8	20	-34	10
S_{38}	$n5d_{xy}$	-20	-3	18	-41	-9	14	-38	11
S_{39}	$n5d_{x^2-y^2}$	-23	-2	21	-50	-9	11	-33	16
S_{40}	$n5d_{z^2}$	-24	-2	19	-44	-8	18	-35	10
S_{41}	?	-22	-1	23	-50	-7	10	-34	11
S_{42}	?	-20	-1	20	-47	-7	9	-32	10
S_{43}	$n7p_x$	-21	-2	20	-39	-10	14	-37	10
S_{44}	$n7p_z$	-20	-1	17	-40	-4	12	-30	8
S_{45}	?	-37	-24	328	-446	-59	-358	22	1
S_{46}	$n7p_y$	-18	1	56	-90	-6	-21	-24	12
S_{47}	?	-23	-3	12	-44	-20	5	-33	20
S_{48}	$\pi\pi^*$	2	38	328	-465	20	-549[a]	41	-3

[a] This value was increased manually from -277 meV to fit the $\pi\pi^*$ potential energy surface to the SOS-ADC(2) one around the $\pi\pi^*/n3p$ intersections.

We note here that two parameters were modified. The ϵ parameter for $n3p_y$ was decreased from 7.14 eV to 7.09 eV (for $n3p_x$ and $n3p_z$, no corrections were necessary). This adjustment produces a vertical excitation energy from the S_0 minimum to the $n3p_y$ state of 7.41 eV (see Table S2), in very good agreement with the experimental value of 7.40 eV.[S3] Additionally, the κ parameter for the $\pi\pi^*$ state and mode 23 was doubled from -519 meV to -1038 meV, in order to make the position of the intersections of $\pi\pi^*$ with the three $n3p$ states agree with the SOS-ADC(2) data.

Figure S6 shows—for a representative scan along the C=O bond length—a comparison between the diabatic LVC potential energy surfaces, the adiabatic LVC potentials that were used to actually run the SHARC simulations, and the reference SOS-ADC(2) potentials. It can be seen that the adiabatic LVC potentials (i.e., after diagonalization of the Hamiltonian including all λ parameters) can faithfully reproduce the shape of the potentials, especially in the relevant region indicated by the grey box. Comparison of panels (a) and (b) also shows that inclusion of the λ parameters leads to the creation of the avoided crossings and significantly affect the shape of some potentials, most notably the $\pi\pi^*$ one.

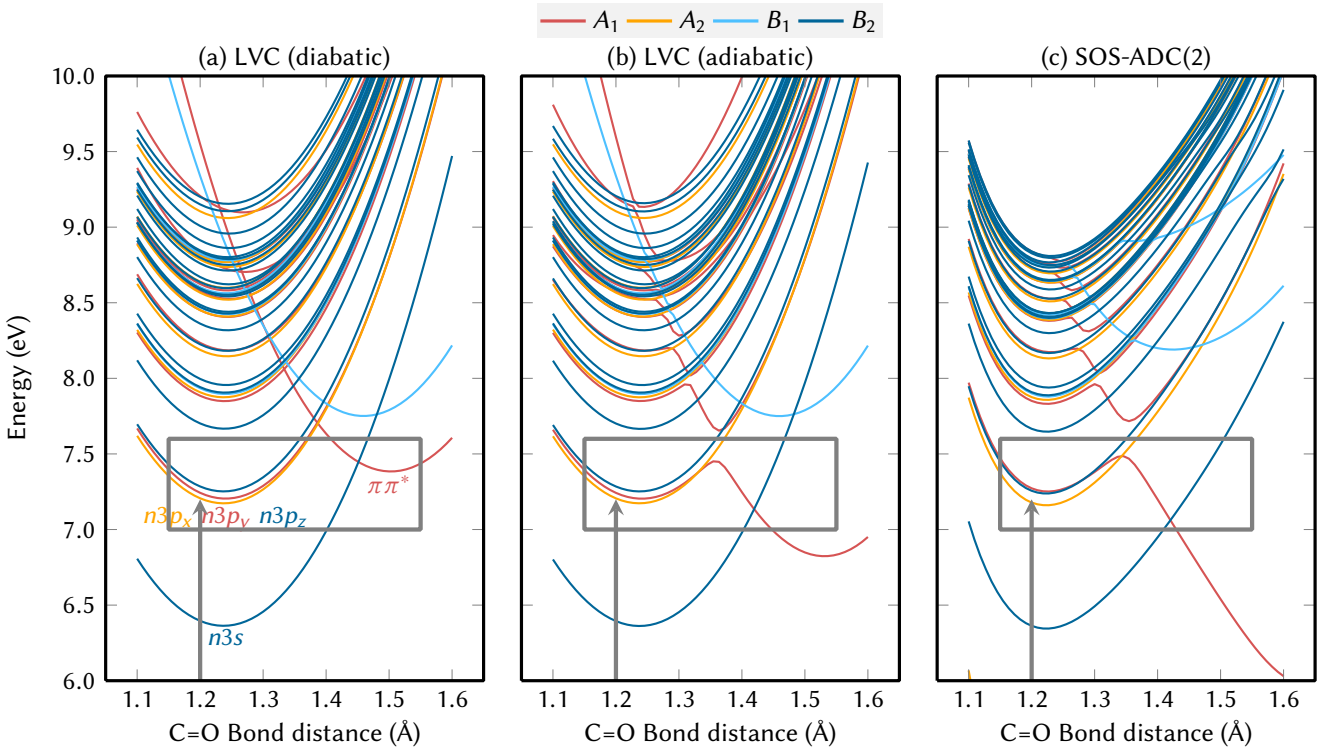

Figure S6: Comparison of potential energy surface scans along the C=O bond length of acetone. (a) shows the diabatic potentials from the LVC model (before including λ parameters). (b) shows the adiabatic potentials from the LVC model after diagonalization. (c) shows the potentials from the SOS-ADC(2) method used for parametrization. Color indicates the irreducible representation of the states (A_1: red, A_2: orange, B_1: light black, B_2: dark black). The grey arrow indicates vertical excitation from the S_0 minimum, the grey box highlights the most relevant parts of the potentials. Note that in this diagram, 0 eV is the energy of S_0 at the n3s minimum and the minimum energy of S_0 is -0.21 eV.

S4.4 Nonadiabatic dynamics simulations

A total of 1000 initial conditions were sampled from the Wigner distribution of the harmonic oscillator of the S_0 state, based on frequencies and normal modes computed at the SOS-MP2 level of theory with the basis set mentioned above. This sampling produced geometries in Cartesian coordinates, which were subsequently converted to the normal-mode basis of the $n3s$ state, in which the LVC model is defined.

To find the initial active states, we carried out a single point calculation with the LVC model for each of these 1000 geometries. In order to selectively excite into the $n3p_x$ Rydberg state, we set the diabatic transition dipole moment between S_0 and $n3p_x$ equal to one and all other transition dipole moments to zero for these single point calculations. Then, the initial active, adiabatic state was found stochastically[S12] in the excitation energy window from 6.77 eV to 8.27 eV. Hence, the initial active state was the adiabatic state that most resembled the $n3p_x$. The initial wave function coefficients were set such that the initial diabatic population of $n3p_x$ was 1. This procedure was then repeated to generate the initial conditions starting in the $n3p_y$ and $n3p_z$ states. The stochastic selection procedure accepted 947 initial conditions for the $n3p_x$ initial state, 929 for the $n3p_y$, and 921 for the $n3p_z$.

All 2797 initial conditions were then propagated for 1000 fs on the coupled 49 potential energy surfaces, using the PySHARC driver.[S5] The nuclear motion was propagated with a 0.5 fs step, and the electronic wave function was integrated with a 0.02 fs step, using the local diabatization scheme.[S13] The required wave function overlaps $\langle\Psi_i(t)|\Psi_j(t+\Delta t)\rangle$ were directly computed as the matrix product of the diabatic-adiabatic transformation matrices of both steps. During a hop, the full momentum vector was rescaled to conserve total energy. An energy-based decoherence correction[S14] (with the standard α parameter of 0.1 atomic units) was applied to the adiabatic wave function coefficients.

S4.5 Electronic population analysis

The LVC model does not describe the minimum region of the $\pi\pi^*$ state fully accurately (see Figure S6), since the minimum is much too shallow. This inaccuracy could lead to trajectories crossing back from the $\pi\pi^*$ state to the Rydberg states. In order to avoid this artificial backflow, trajectories were scanned for hops from the $\pi\pi^*$ state to higher states and truncated to 10 fs before this backhop occurs. In this way, the $\pi\pi^*$ population is monotonically increasing, which is consistent with the expected behavior in the much deeper $\pi\pi^*$ potential energy surface described by SOS-ADC(2) (see Figure S6b).

The trajectory data was analyzed by means of the diabatic electronic populations. These were obtained by an adiabatic-diabatic transformation:

$$c_\alpha^{\mathrm{diab}}(t_i) = \sum_\beta U_{\alpha\beta}(t_i) c_\beta^{\mathrm{adiab}}(t_i), \tag{15}$$

with

$$\mathbf{U}(t_i) = \mathbf{T} \cdot \prod_{j=1}^{i} \mathbf{S}(t_{j-1}, t_j), \tag{16}$$

$$S_{\alpha\beta} = \left\langle \Psi_\alpha^{\mathrm{adiab}}(t_{j-1}) \middle| \Psi_\beta^{\mathrm{adiab}}(t_j) \right\rangle, \tag{17}$$

$$T_{\alpha\beta} = \left\langle \Psi_\alpha^{\mathrm{diab}}(0) \middle| \Psi_\beta^{\mathrm{adiab}}(0) \right\rangle, \tag{18}$$

where the matrix product in the first line was computed in a time-ordered fashion. This transfor-

mation yields for each trajectory j the diabatic coefficients $c_{\alpha,j}^{\mathrm{diab}}(t_i)$, which are then incoherently averaged to give the total population of diabatic state α:

$$P_{\alpha}^{\mathrm{diab}}(t_i) = \frac{1}{N_{\mathrm{traj}}} \sum_{j}^{N_{\mathrm{traj}}} \left| c_{\alpha,j}^{\mathrm{diab}}(t_i) \right|^2 . \tag{19}$$

This averaging is independently done for each of the three ensembles (with initial state $n3p_x$, $n3p_y$, or $n3p_z$).

S4.6 Fitting of the electronic populations

Since the diabatic model includes 49 electronic states, we obtain 49 population curves from the diabatization. However, only four states are appreciably populated: $n3p_x$, $n3p_y$, $n3p_z$, and $\pi\pi^*$. The other states are nevertheless necessary to improve the description of the potential energy surfaces of the n3p states of the more strongly coupled $\pi\pi^*$ state, but are generally weakly populated. Hence, to simplify the population analysis, the population of all remaining states is summed with the $\pi\pi^*$ state, and one single label is used.

The population data with 3×4 states was then fitted in a global procedure with the solution of equation (1). Because in the simulations, no explicit pump laser was used, the source term $g(t)$ is 1 at $t = 0$ and zero everywhere else. This simplifies equation (4) to:

$$\vec{P}(t) = e^{\mathbf{M}t} \cdot \vec{P}_0 \tag{20}$$

for $t \geq 0$. In accord with the employed initial conditions, the $\vec{P}_0$ vector was simply $P_0^{n3p_x} = (1, 0, 0, 0)$, $P_0^{n3p_y} = (0, 1, 0, 0)$, or $P_0^{n3p_z} = (0, 0, 1, 0)$. For the actual fitting procedure, equation (20) was solved numerically with the Runge-Kutta 5(4) algorithm[S15] with suitable initial guesses for all time constants (τ_{xy}, τ_{xz}, τ_{yx}, τ_{yz}, τ_{zx}, τ_{zy}, $\tau_{x\pi}$, $\tau_{y\pi}$, and $\tau_{z\pi}$). The time constants were then optimized with the "Trust Region Reflective" algorithm[S16] implemented in SciPy, which was employed to restrain all time constants to be positive. By diagonalizing the coupling matrix $\mathbf{M}$ with the optimized time constants, we obtain the simulated eigenvalues λ_m, which can also be converted to the effective time constants by $\tau_m = \lambda_m^{-1}$.

To estimate the errors in the obtained time constants, we employed the bootstrapping method,[S17,S18] where we generated 1000 copies of the ensemble population data by random resampling with replacement (i.e., in the resamples some trajectories appear several times and others do not). These 1000 copies were fitted to the same kinetic model, yielding 1000 realizations of the time constants. From the histograms of these realizations, the fitting errors given in the manuscript were obtained as the arithmetic standard deviations (for $\tau_{x\pi}$, the multiplicative geometric standard deviation σ_g is shown as $\mathrm{mean}^{+\mathrm{mean}(\sigma_g - 1)}_{\mathrm{mean}(\sigma_g^{-1} - 1)}$). To estimate the error in the time constants derived from the eigenvalues, the coupling matrix was diagonalized for each realization of the fitted time constants and the histograms of the resulting effective time constants analyzed.

S4.7 Energy-dependent analysis

The sampling of the initial conditions from the Wigner distribution leads to a set of geometry snapshots with different kinetic and potential energies. On average, the kinetic and potential energy of the sampled ground state agrees with the zero-point energy, but each individual snapshot can have kinetic and/or potential energy above/below the zero-point energy. This distribution of energies is presented in Figure S7. Panel (a) shows the uncorrelated distribution of kinetic and potential

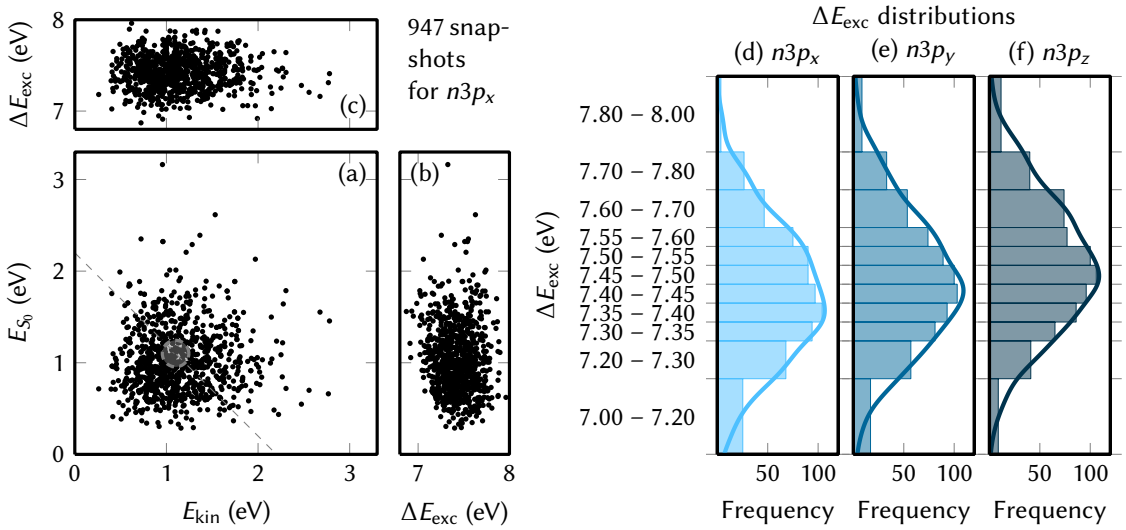

Figure S7: Plots of the distribution of energies in the initial condition snapshots. (a)–(c) Scatter plots of the kinetic energy E_{kin}, the ground state potential energy E_{S_0}, and the excitation energy ΔE_{exc} for the $n3p_x$ initial conditions, showing the spread of these energetic values. In (a), the dashed line and grey circle indicate the zero-point energy of about 2.2 eV. (d)–(f) Histograms of the distribution of excitation energy ΔE_{exc} of the initial conditions. The shown energy windows are the basis of the energy-resolved analysis of the population dynamics.

energy. Panels (b) and (c) also show the distribution of the excitation energies (exemplarily for $n3p_x$). The distributions of excitation energies for all three ensembles is shown in panels (d) to (f).

The rather broad distribution of excitation energies in the initial condition hampers the direct comparison of the full ensemble results with experiment because the latter excites only to a narrow window of excitation energy. Hence, the full ensemble results should be understood as average results, which should be compared to the average of the experimental results for different energies. However, the broad excitation distribution allows us to easily perform an energy-resolved analysis. For this analysis, the excitation energy was binned into 11 intervals (with 7.0–7.2 eV being the first one, and 7.8–8.0 eV the last one, see Figure S7d–f). For each of these intervals, the electronic populations were independently extracted and fitted according to the protocol presented above. Thus, the fitting protocol provides the 9 fitting parameters for each energy interval separately, allowing the observation of an energy-dependence of the time constants. Also for these time constants, we computed the effective time constants via diagonalization of the coupling matrix. Figures S9 to S19 present the global population fits for the individual energy ranges.

S5 Additional Computational Results

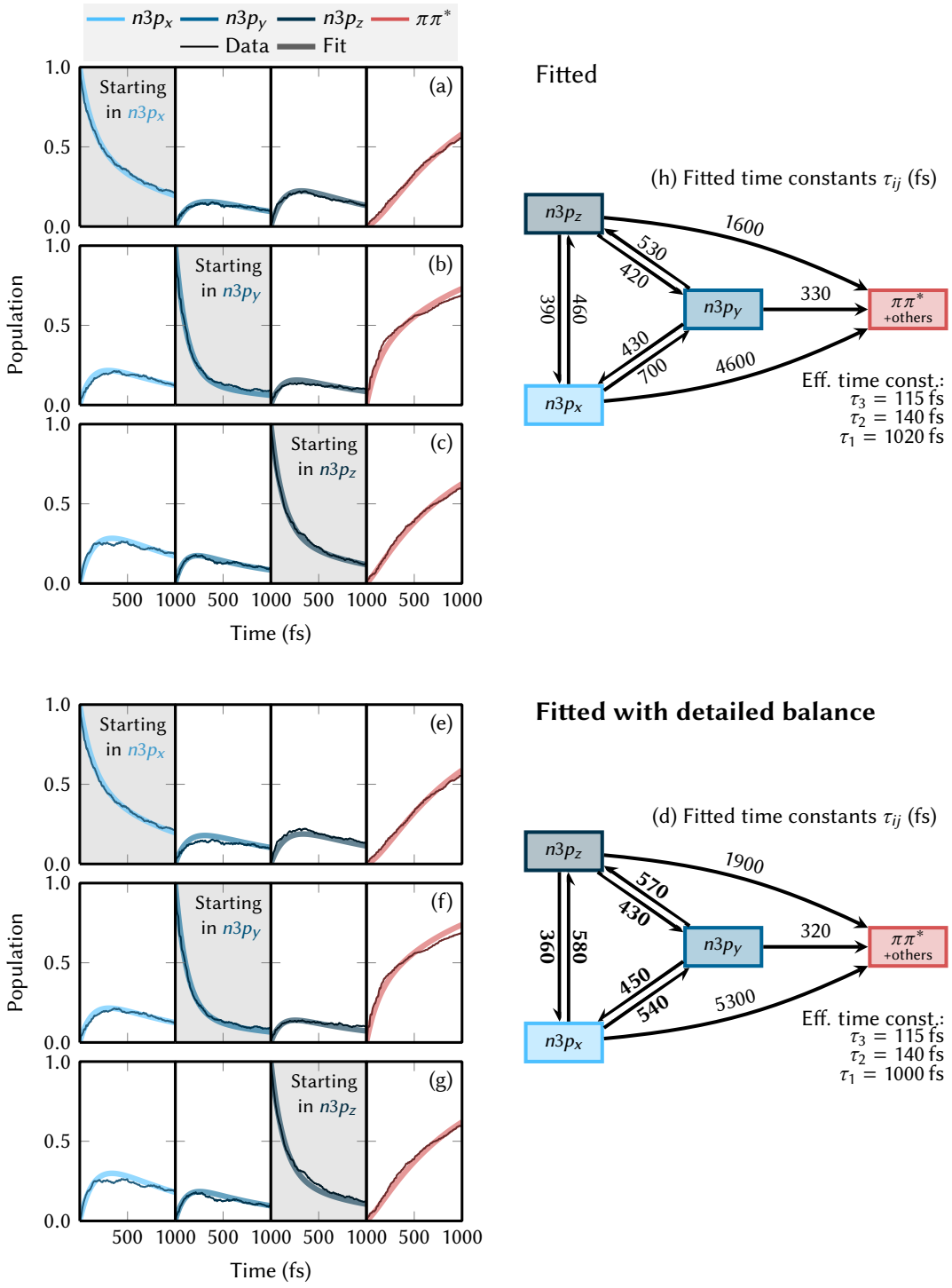

Figure S8: (a)–(d) Global fit of the electronic populations with nine independent time constants (identical with Figure 3). (e)–(h) Global fit with six independent time constants, where the ratios between back- and forth reactions (i.e., τ_{xy}/τ_{yx}, τ_{xz}/τ_{zx}, and τ_{yz}/τ_{zy}) were held constant at $\frac{\tau_{ij}}{\tau_{ji}} = \exp(-\frac{E_i - E_j}{k_B T_{\text{eff}}})$ ($T_{\text{eff}} = 2500\,\text{K}$) such that the time constants obey detailed balance. The constrained fit is almost as good ($\chi^2 = 5.9$) as the unconstrained fit ($\chi^2 = 3.6$), and most time constants (except τ_{xy} and τ_{xz} are within the error estimate of the unconstrained fit.

Table S4 collects all obtained time constants for the full ensemble and for the different energy ranges. Table S5 gives the number of trajectories within each full ensemble and for the energy ranges.

Table S4: Fitted time constants for the full ensemble with error estimates (from bootstrapping) and for the different energy ranges (all in fs). The sum of square residuals (χ^2) are also given.

Energy range	τ_{xy}	τ_{xz}	τ_{yx}	τ_{yz}	τ_{zx}	τ_{zy}
Full ensemble	701±56	455±30	430±29	533±43	395±28	417±26
7.0 – 7.2 eV	1012	488	362	527	385	345
7.0 – 7.3 eV	810	459	482	465	370	344
7.3 – 7.35 eV	660	420	273	2252	408	581
7.35 – 7.4 eV	698	583	472	664	418	477
7.4 – 7.45 eV	607	647	589	540	434	414
7.45 – 7.5 eV	917	703	570	433	645	389
7.5 – 7.55 eV	1086	403	434	577	428	404
7.55 – 7.6 eV	433	303	372	485	240	594
7.6 – 7.7 eV	613	500	504	525	327	519
7.7 – 7.8 eV	1037	261	370	479	298	287
7.8 – 8.0 eV	1898	279	975	289	237	423

Energy range	$\tau_{x\pi}$	$\tau_{y\pi}$	$\tau_{z\pi}$	$\Re(\tau_1)$	$\Re(\tau_2)$	$\Re(\tau_3)$	χ^2
Full ensemble	4605^{+5266}_{-2600}	329±22	1567±360	1015±26	142±6	116±4	3.63
7.0 – 7.2 eV	2475	942	1454	1560	153	122	12.13
7.0 – 7.3 eV	∞	762	891	1527	162	113	10.28
7.3 – 7.35 eV	2581	512	2076	1282	140[a]	140[a]	13.86
7.35 – 7.4 eV	3076	389	∞	1314	166	136	8.53
7.4 – 7.45 eV	2285	417	4124	1074	167	131	9.63
7.45 – 7.5 eV	∞	248	1756	1077	201	106	13.59
7.5 – 7.55 eV	1584	300	20,061	1033	142	121	12.72
7.55 – 7.6 eV	1761	239	1377	719	101	96	9.93
7.6 – 7.7 eV	1892	172	4217	743	139	95	4.87
7.7 – 7.8 eV	877	176	1532	538	93	89	9.95
7.8 – 8.0 eV	378	150	∞	490	103	78	29.9

[a] Complex eigenvalues with small (< 10%) imaginary components.

Table S5: Number of trajectories in each ensemble and each energy range.

Energy range	$N^{\mathrm{traj}}_{n3p_x}$	$N^{\mathrm{traj}}_{n3p_y}$	$N^{\mathrm{traj}}_{n3p_z}$
Full ensemble	947	929	921
7.0 – 7.2 eV	101	68	35
7.0 – 7.3 eV	136	114	82
7.3 – 7.35 eV	94	81	65
7.35 – 7.4 eV	104	93	86
7.4 – 7.45 eV	97	103	96
7.45 – 7.5 eV	90	100	106
7.5 – 7.55 eV	90	89	100
7.55 – 7.6 eV	75	74	77
7.6 – 7.7 eV	93	107	148
7.7 – 7.8 eV	53	66	80
7.8 – 8.0 eV	14	34	46

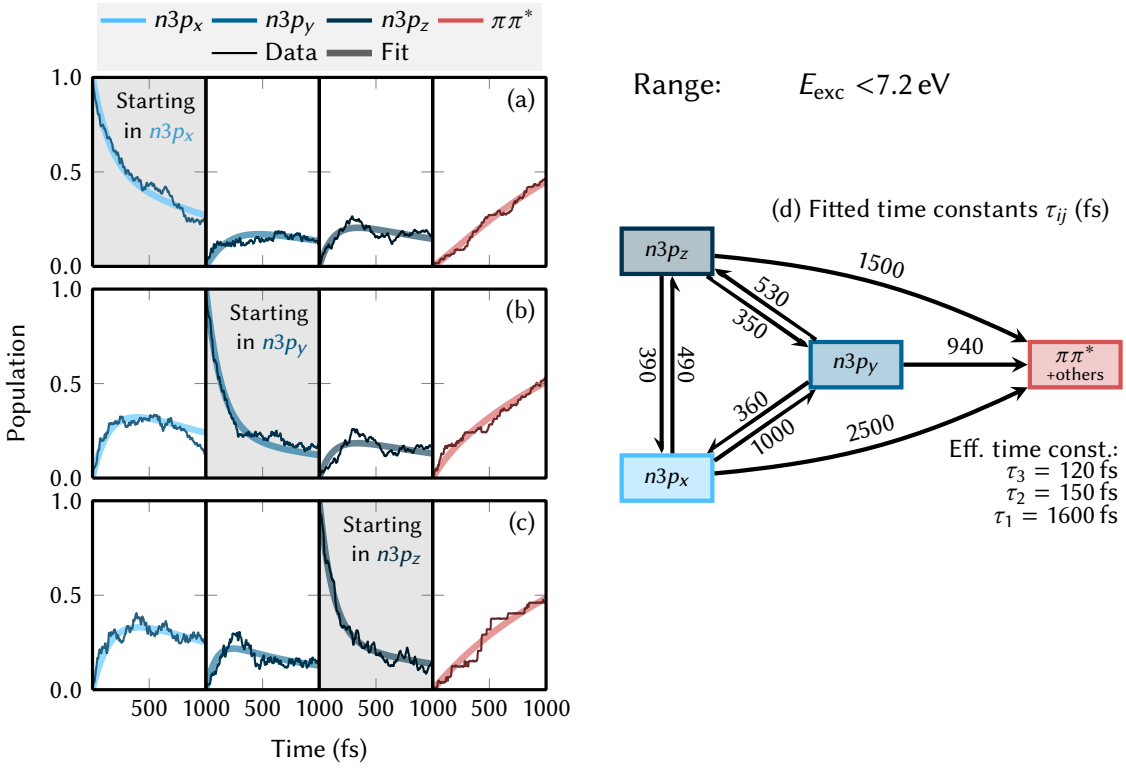

Figure S9: Results of the global fit of the electronic populations in the energy range 7.0–7.2 eV.

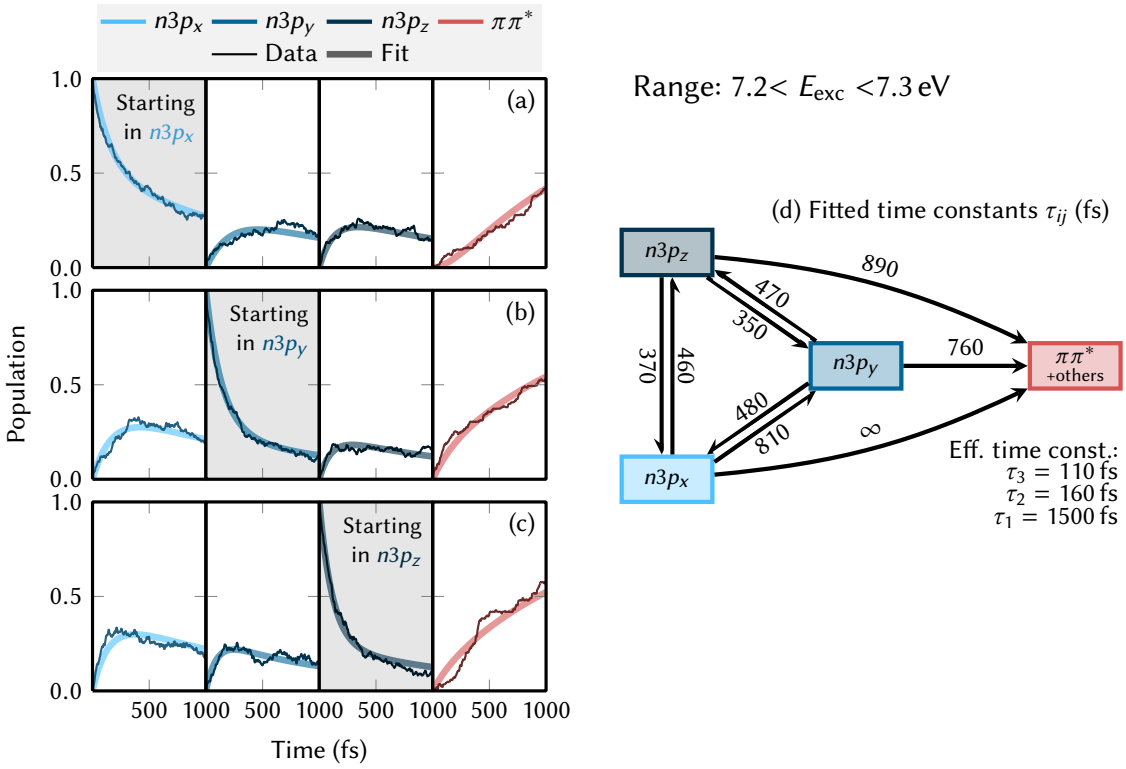

Figure S10: Results of the global fit of the electronic populations in the energy range 7.2–7.3 eV.

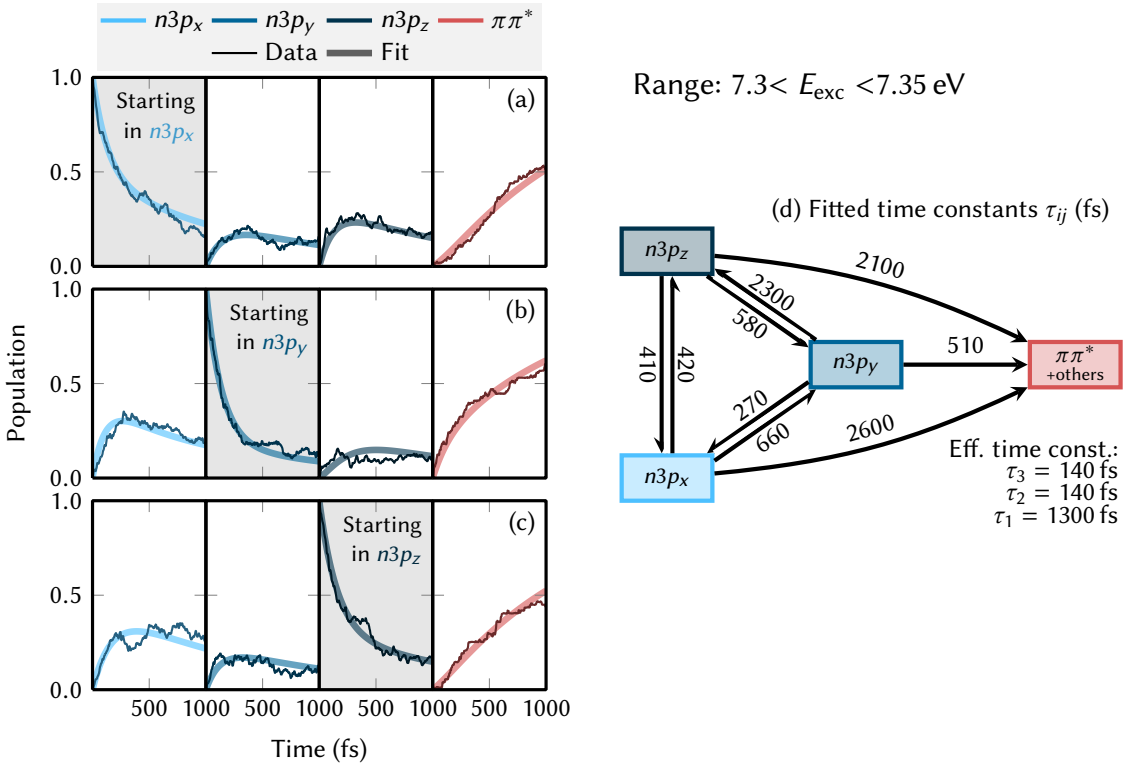

Figure S11: Results of the global fit of the electronic populations in the energy range 7.3–7.35 eV.

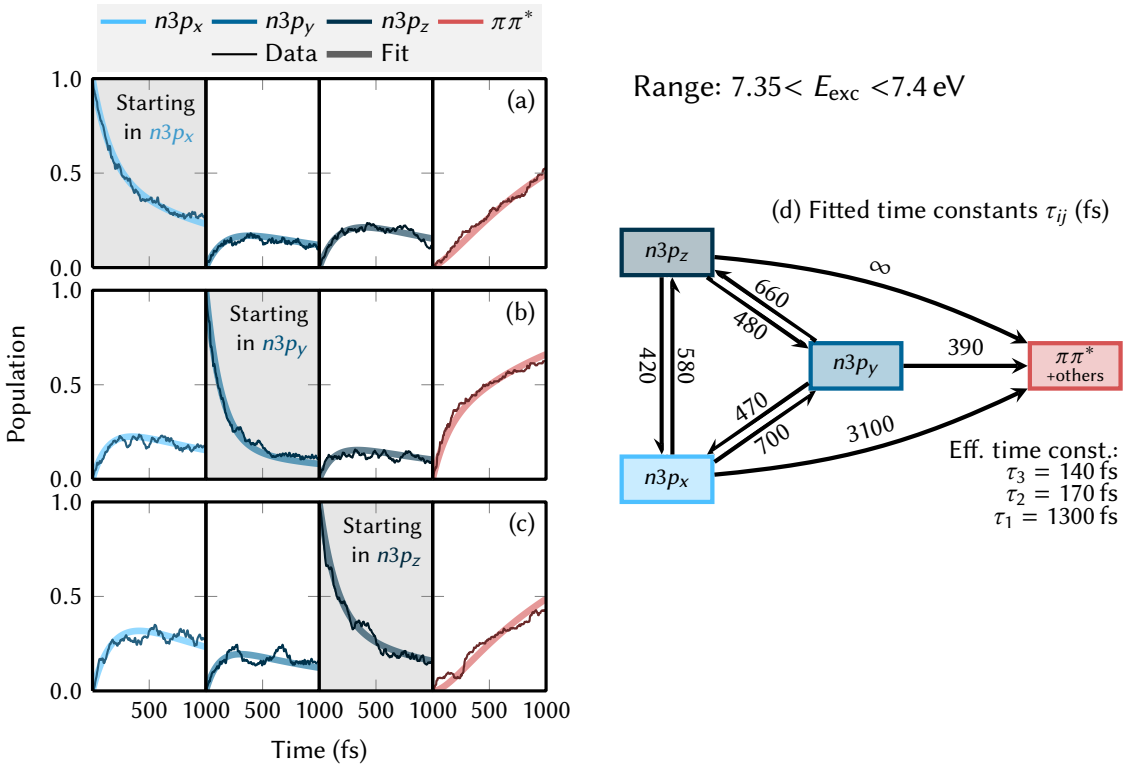

Figure S12: Results of the global fit of the electronic populations in the energy range 7.35–7.4 eV.

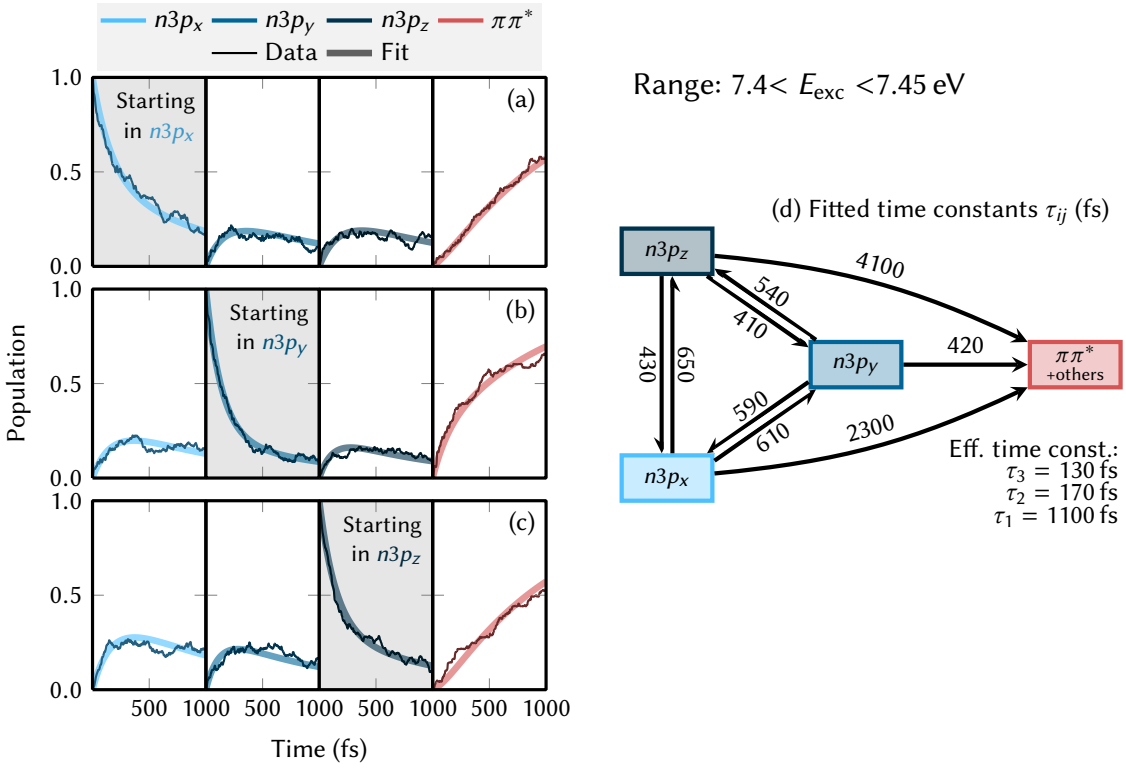

Figure S13: Results of the global fit of the electronic populations in the energy range 7.4–7.45 eV.

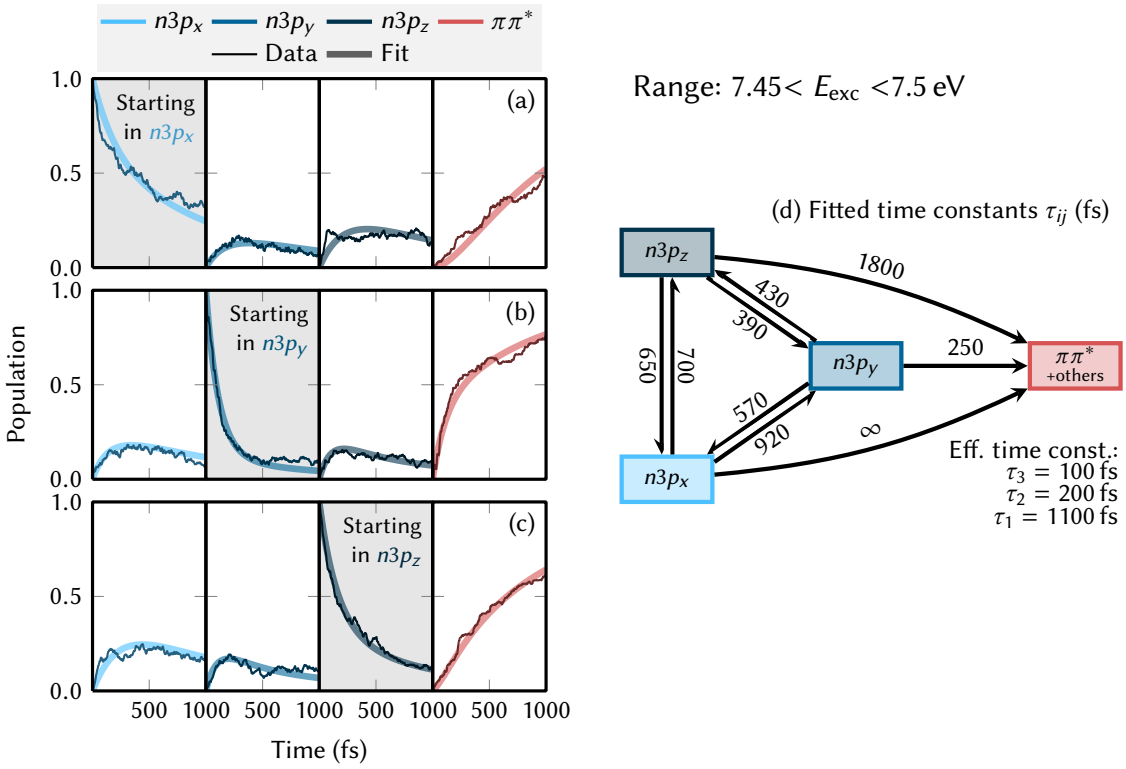

Figure S14: Results of the global fit of the electronic populations in the energy range 7.45–7.5 eV.

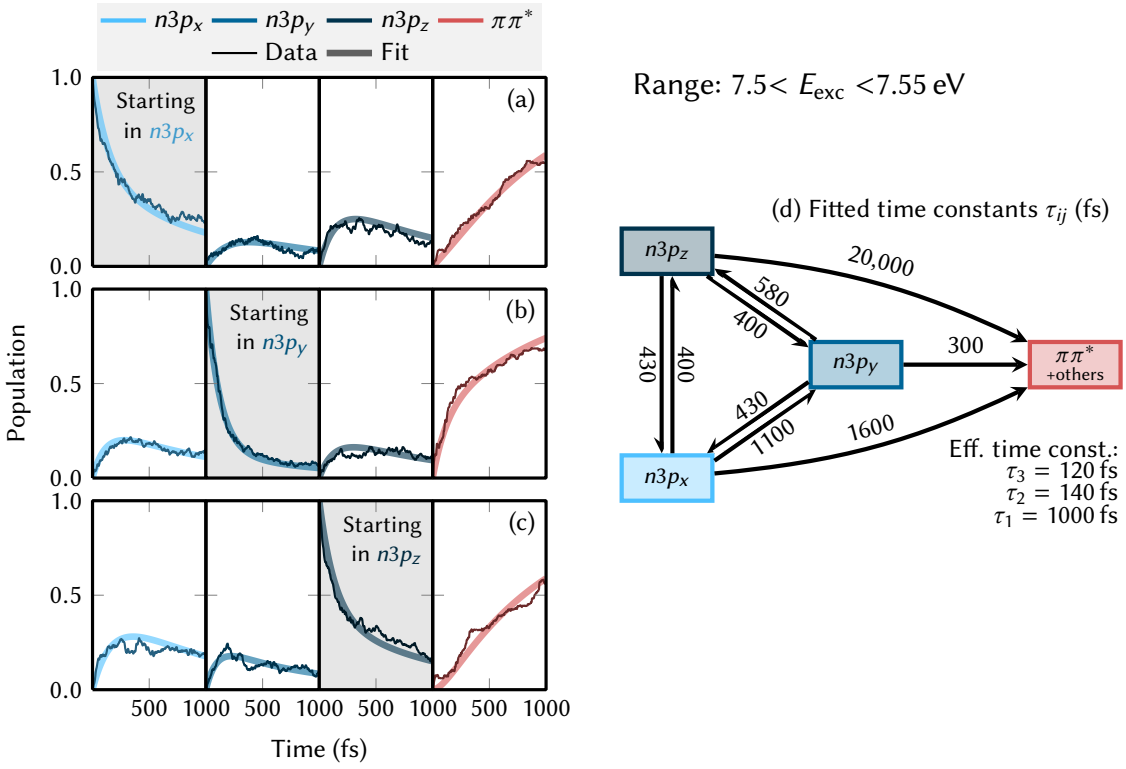

Figure S15: Results of the global fit of the electronic populations in the energy range 7.5–7.55 eV.

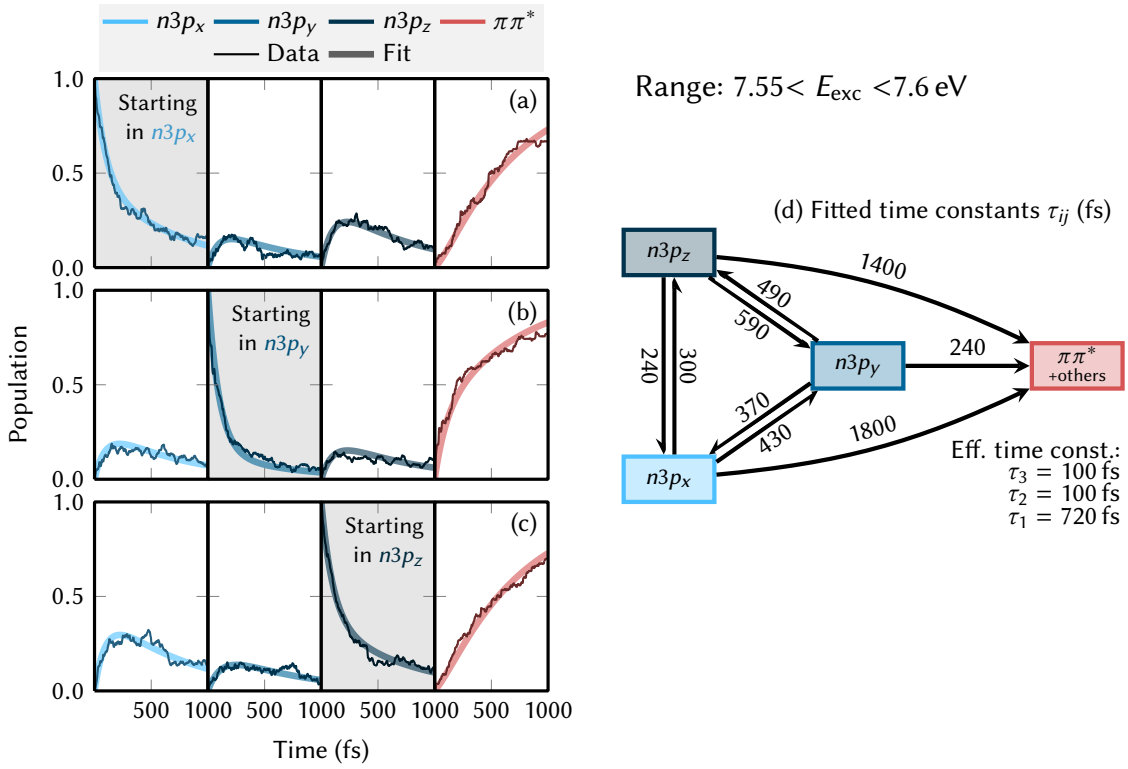

Figure S16: Results of the global fit of the electronic populations in the energy range 7.55–7.6 eV.

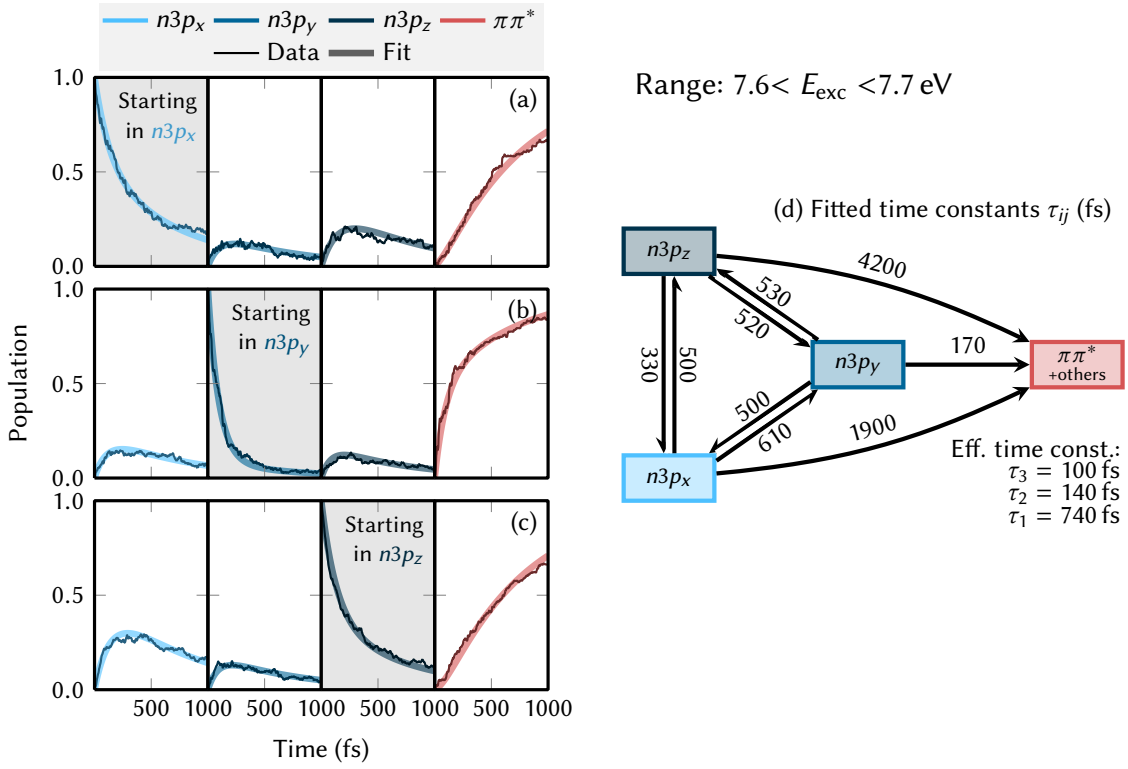

Figure S17: Results of the global fit of the electronic populations in the energy range 7.6–7.7 eV.

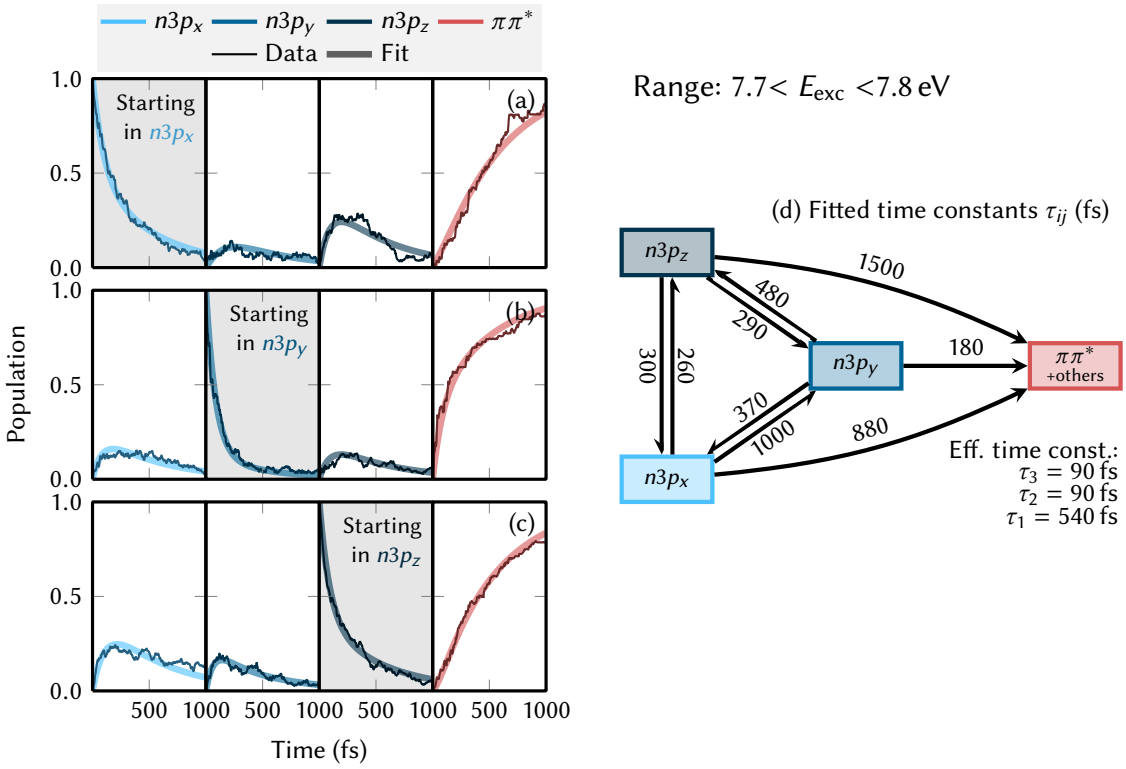

Figure S18: Results of the global fit of the electronic populations in the energy range 7.7–7.8 eV.

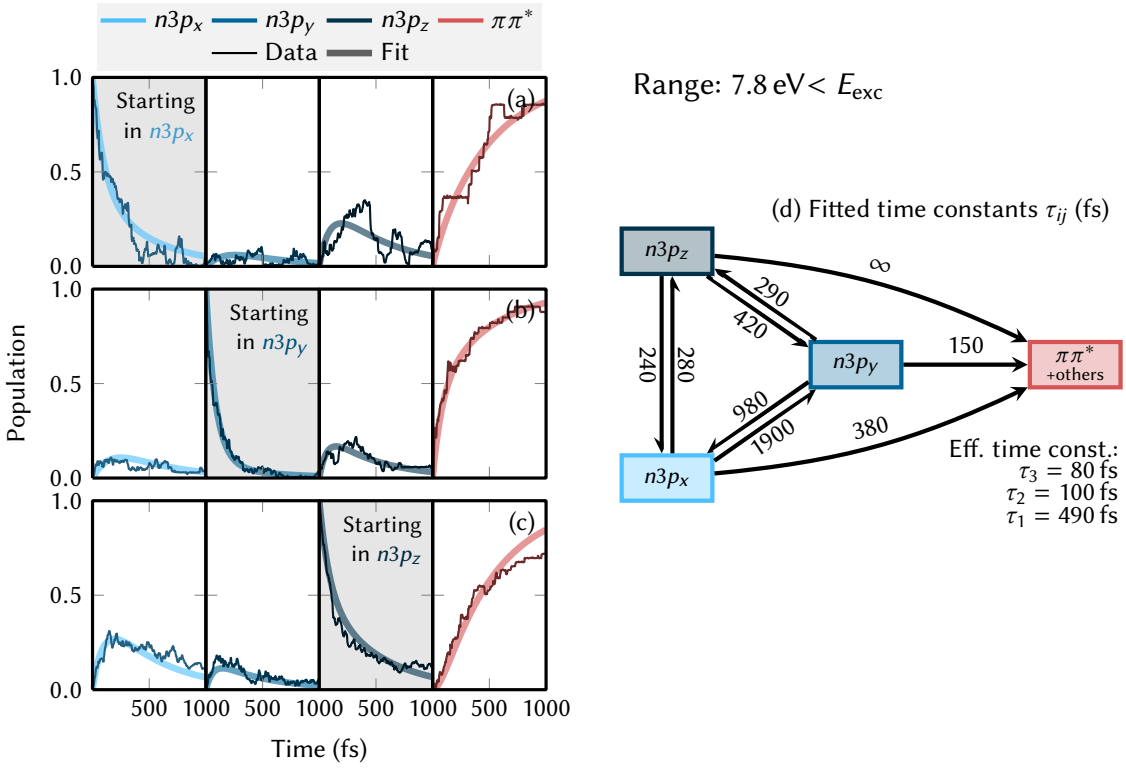

Figure S19: Results of the global fit of the electronic populations in the energy range 7.8–8.0 eV.

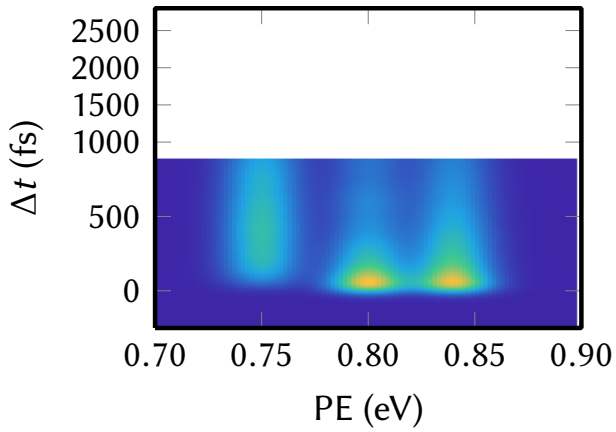

Figure S20: Time-resolved photoelectron spectrum simulated from the diabatic populations obtained with the SHARC computations (0.52 times the ensemble starting in n3p$_y$ plus 0.48 times the ensemble starting in n3p$_z$). The spectrum assumes identical photoionization probabilities for all three Rydberg states.

References

(S1) van Stokkum, I. H.; Larsen, D. S.; van Grondelle, R. *Biochem. Biophys. Acta Bioenergetics* **2004**, *1657*, 82 – 104.

(S2) Wu, G.; Boguslavskiy, A. E.; Schalk, O.; Schuurman, M. S.; Stolow, A. *J. Chem. Phys.* **2011**, *135*, 164309.

(S3) Nobre, M.; Fernandes, A.; da Silva, F. F.; Antunes, R.; Almeida, D.; Kokhan, V.; Hoffmann, S. V.; Mason, N.; Eden, S.; Limão-Vieira, P. *Phys. Chem. Chem. Phys.* **2008**, *10*, 550–560.

(S4) Köppel, H.; Domcke, W.; Cederbaum, L. S. *Adv. Chem. Phys.*; John Wiley & Sons, Inc., 1984; Vol. 57; pp 59–246.

(S5) Plasser, F.; Goméz, S.; Mai, S.; González, L. *Phys. Chem. Chem. Phys.* **2019**, *21*, 57–69.

(S6) Dreuw, A.; Wormit, M. *WIREs Comput. Mol. Sci.* **2015**, *5*, 82–95.

(S7) Dunning, T. H. *J. Chem. Phys.* **1989**, *90*, 1007–1023.

(S8) Kaufmann, K.; Baumeister, W.; Jungen, M. *J. Phys. B: At. Mol. Phys.* **1989**, *22*, 2223.

(S9) TURBOMOLE V7.0, A development of University of Karlsruhe and Forschungszentrum Karlsruhe GmbH. 2015.

(S10) Fumanal, M.; Plasser, F.; Mai, S.; Daniel, C.; Gindensperger, E. *J. Chem. Phys.* **2018**, *148*, 124119.

(S11) Plasser, F.; Ruckenbauer, M.; Mai, S.; Oppel, M.; Marquetand, P.; González, L. *J. Chem. Theory Comput.* **2016**, *12*, 1207.

(S12) Barbatti, M.; Granucci, G.; Persico, M.; Ruckenbauer, M.; Vazdar, M.; Eckert-Maksić, M.; Lischka, H. *J. Photochem. Photobiol. A* **2007**, *190*, 228–240.

(S13) Granucci, G.; Persico, M.; Toniolo, A. *J. Chem. Phys.* **2001**, *114*, 10608–10615.

(S14) Granucci, G.; Persico, M. *J. Chem. Phys.* **2007**, *126*, 134114.

(S15) Dormand, J.; Prince, P. *J. Comput. Appl. Math.* **1980**, *6*, 19 – 26.

(S16) Branch, M.; Coleman, T.; Li, Y. *SIAM J. Sci. Comput.* **1999**, *21*, 1–23.

(S17) Nangia, S.; Jasper, A. W.; Miller, T. F.; Truhlar, D. G. *J. Chem. Phys.* **2004**, *120*, 3586–3597.

(S18) Mai, S.; Marquetand, P.; González, L. *J. Phys. Chem. Lett.* **2016**, *7*, 1978–1983.